Available online at www.sciencedirect.com

ScienceDirect

Geochimica et Cosmochimica Acta 304 (2021) 160–177

Geochimica et Cosmochimica Acta

www.elsevier.com/locate/gca

Potassium isotopic fractionation during clay adsorption

Wenshuai Li [a], Xiao-Ming Liu [a,*], Yan Hu [b], Fang-Zhen Teng [b], Yongfeng Hu [c]

[a] Department of Geological Sciences, University of North Carolina-Chapel Hill, NC 27599-3315, USA
[b] Isotope Laboratory, Department of Earth and Space Sciences, University of Washington, Seattle, WA 98195-1310, USA
[c] Canadian Light Source, University of Saskatchewan, Saskatoon S7N 2V3, Canada

Received 21 September 2020; accepted in revised form 22 April 2021; available online 29 April 2021

Abstract

Clay adsorption is a critical process responsible for the mobilization and cycling of potassium (K) on Earth's surface. Recent studies emphasized the potential of using stable K isotopes ($\delta^{41}K$) to understand chemical weathering. However, the direction, degree, and mechanism of K isotopic fractionation linked to clay K uptake during chemical weathering remain poorly constrained. This work investigated the mechanism of K adsorption on clays (kaolinite and smectite) and the isotopic fractionation in three experimental sets with K-containing solutions. The time-series experiments revealed that the adsorption and isotope equilibria were attained after less than 12-hour reaction. Potassium adsorption rate slowed down and its isotopic fractionation approached the steady-state during 15-day reaction. The pH-dependent experiments demonstrated that the percentage of clay K adsorption and the isotopic composition of adsorbed K (and aqueous K) display negative linear correlations. Net isotopic fractionation between adsorbed and aqueous phases ($\Delta^{41}K_{ad\text{-}aq}$) remained near-constant (0.6–0.8‰), regardless of variations in pH ranging from 4 to 10. The concentration-control experiments demonstrated that the percentage of K adsorption decreased with increasing KCl concentrations from 0.005 to 20 mM. The $\delta^{41}K$ values of aqueous K reached the minimum of −0.53‰ after 92.7% K adsorbed (initial KCl of 0.005 mM). Potassium adsorption was substantially suppressed as ionic strength (fixed by Na^+) increased from 0.001 to 0.5 M without apparent $\Delta^{41}K_{ad\text{-}aq}$ variations. The K *K*-edge XANES demonstrated that primary K incorporated in clay lattice and surface KCl derived from sorbed K^+ and Cl^- synchro-dehydration can be identified after drying of clays. These features indicate that adsorbed K^+ was bounded onto clays as outer-sphere complexes, which can be replaced with excess Na^+ at high ionic strength. Based on experimental results, we cannot distinguish specific mineralogy regulation on K isotopic fractionation. In sum, isotopically heavy K is preferentially sorbed on clay minerals. The results confirm an equilibrium fractionation path independent of reaction time, pH, ionic strength, and initial KCl concentration. Observed K isotopic fractionation is best fitted by an equilibrium isotopic fractionation law with a fractionation factor $\alpha_{ad\text{-}aq}$ of 1.00075. We highlight the opposite direction of K isotopic fractionation in clay adsorption and structural incorporation during chemical weathering, and their comparative contributions should be considered for future field investigations.

Keywords: Potassium isotope; Adsorption experiment; Clay incorporation; Kaolinite; Smectite; Chemical weathering; XANES

1. INTRODUCTION

Continental weathering of silicate rocks is one of the driving forces for multiple Earth's surface processes, including (i) shaping planetary topography, (ii) promoting pedogenesis, (iii) linking the element cycles between the lithosphere and the biosphere, and (iv) regulating atmospheric CO_2 levels and carbon cycles (e.g., Kump et al., 2000; Amiotte Suchet et al., 2003; Berner and Berner, 2012). From global perspectives, potassium (K) is a major element (~1.8%) in the crust and can be easily mobilized and leached during

* Corresponding author.
E-mail address: xiaomliu@unc.edu (X.-M. Liu).

https://doi.org/10.1016/j.gca.2021.04.027
0016-7037/

the dissolution of silicate rocks and subsequent transport into river runoffs through weathering alteration over time (Li and Yang, 2010; Rudnick and Gao, 2013; S. Li et al., 2019; Wang et al., 2020a). Furthermore, K is known as one of the essential macronutrients for plant growth and development (Tripler et al., 2006; Sardans and Peñuelas, 2015). Chemical weathering and biological cycling are dominant drivers for stable isotopic fractionation at Earth's surface, controlling global elemental and isotopic budgets (e.g., Anbar and Rouxel, 2007; Liu et al., 2013; Teng et al., 2017). There are two stable K isotopes: ^{39}K (abundance of 93.26%) and ^{41}K (abundance of 6.73%), and their isotope ratios are expressed as $\delta^{41}K$ (in per-mille). Recent advances in the analysis of K isotope ratios using multi-collector inductively-coupled plasma mass spectrometry (MC-ICP-MS) can produce high-precision K isotope data with analytical precisions up to 0.06‰ (2 S.D.) (Li et al., 2016; Wang and Jacobsen, 2016; Morgan et al., 2018; Hu et al., 2018; Chen et al., 2019; X. Li et al., 2020; Moynier et al., 2021). Hence, distinct K isotopic compositions in various K reservoirs on Earth's surface can be better characterized, calling for the use of K isotopes as a promising proxy for global K cycling.

The oceanic K budget is regulated by the mass balance of K inputs from continental runoffs (and/or groundwater discharges), hydrothermal contributions, and K sequestration by marine authigenic minerals (S. Li et al., 2019; Hu et al., 2020). A better understanding of low-temperature K isotopic fractionation helps to characterize K isotope mass fluxes, sources, and sinks on a global scale, which is critical for constraining K cycles at Earth's surface (e.g., S. Li et al., 2019; Chen et al., 2020; Santiago Ramo et al., 2020; Sun et al., 2020; Teng et al., 2020). Currently, it is known that terrestrial materials (usually rich in secondary minerals) have lighter K isotopic composition (e.g., the upper continental crust, averaged $\delta^{41}K$ of -0.44 ± 0.05‰, Huang et al., 2020) than that of the modern seawater ($\delta^{41}K$ of ~0.14‰, Hille et al., 2019; Wang et al., 2020b). Therefore, stable K isotopes have the potential to decipher various fluid-rock interactions (S. Li et al., 2019; Hille et al., 2019; Chen et al., 2020; Huang et al., 2020; Teng et al., 2020; Wang et al., 2020a; Li et al., 2021a). Despite substantial efforts in clarifying K isotopic fractionation in Earth's surface systems, including hydrothermally altered oceanic crust (Parendo et al., 2017; Santiago Ramo et al., 2020), subduction zones (Hu et al., 2020, 2021; Liu et al., 2020), marine sediments (and pore waters) (Santiago Ramos et al., 2018; 2020), weathering profiles (Chen et al., 2020; Teng et al., 2020), rivers (S. Li et al., 2019; Wang et al., 2020a), plants (Christensen et al., 2018), and carbonates (Li et al., 2021b), a full appreciation of physicochemical processes controlling K isotopic fractionation remains elusive.

Potassium isotopes have the potential to trace (bio)geochemical K cycles, but first, the dominant processes driving isotopic fractionation between different K reservoirs on Earth's surface should be understood. Previous studies on natural K biogeochemical cycles reveal that the fate of K is largely modulated by the cation exchange process (adsorption) in terrestrial environments (Pal et al., 1999). Despite rapid clay formation promoting structural incorporation (Michalopoulos and Aller,1995; Rahman, 2019), a few recent studies have examined the fate of K in aquifers and soils and emphasized the importance of clay exchangeable K (Griffioen, 2001; Chaudhuri et al., 2007; Simonsson et al., 2016). Among several processes that fractionate stable metal isotopes (e.g., Ni, Zn, Li, Mo, Ca, and W) at the interface between river water/seawater and clays/oxides, adsorption is regarded as one of the principal causes (e.g., Pokrovsky et al., 2005; Balistrieri et al., 2008; Wasylenki et al., 2014, 2020; Goldberg et al., 2009; Bryan et al., 2015; D. Li et al., 2015; Spivak-Birndorf et al., 2018; Brazier et al., 2019; Li and Liu, 2020). Generally, cations could be bound to various surfaces of clays, including (i) external basal surfaces (permanently charged), (ii) external edge sites (pH-dependent charged sites such as aluminol and silanol hydroxyls), and (iii) accessible interlayer space (Uddin, 2017). Outer-sphere complexation (physisorption, electrostatic interaction) and inner-sphere complexation (chemisorption, covalent/ionic bonding) generally form, which may cause isotopic fractionation of various levels. Experimental studies help to understand isotopic fractionations in well-constrained conditions. Compared with well-studied isotope tracers of weathering such as Li and Mg (Teng et al., 2017), little is known about K isotopic fractionation associated with clay adsorption during weathering. The adsorption of K on absorbents may result in large differences in K isotopic compositions between sorbed and aqueous phases. Clay adsorption experiments may provide insights into (bio)geochemical K cycles and decipher Earth's surface processes using K isotopes.

This study aims to understand the mechanisms of K isotopic fractionation during uptake by clays. We focused on the pathway of K removal from fluids during adsorption on clay particles. We further compared how K isotopes fractionate differently during clay adsorption and structural incorporation. Specifically, we determined the isotopic fractionation between sorbed K (K_{ad}) and aqueous K (K_{aq}) based on experimental constraints in the closed system where K^+ adsorption occurred on two common clay minerals (kaolinite and smectite). The objectives of this study are to investigate: (i) the amount of sorbed K and the mode of complexation on clays under various environmental conditions; (ii) the direction, magnitude, and mechanism of isotopic fractionation between aqueous K and adsorbed K; and (iii) potential environmental factors (as adsorbents, pH, ionic strength, and adsorption ratio) controlling isotopic fractionation during clay adsorption; (iv) K isotopic fractionation patterns during clay adsorption compared with structural incorporation in clays, where we quantified the K isotopic fractionation between dissolved and sorbed phases and examined atomic coordination environments. This study helps to improve our understanding of the processes and mechanisms controlling K isotopic compositions of sediments and waters.

2. EXPERIMENT SETUP

2.1. Starting materials

This study focused on K adsorption onto common naturally occurring clay minerals, including kaolinite and

smectite, which allow for the first-order analogy with natural environments. Well-characterized clay reference materials (kaolinite KGa-2 and smectite SWy-2) were purchased from the Clay Mineral Society (CMS), which have been widely reported in the literature (Kosmulski, 2011; D. Li et al., 2015; Guinoiseau et al., 2016; Brazier et al., 2019). Critically, these clay samples were processed to recover clay-sized fractions (0.1–1 μm) and eliminate surface impurities and labile components to avoid possible errors during chemical analyses. Hence, we used a modified washing protocol reported in Guinoiseau et al. (2016) and Brazier et al. (2019). In brief, clays were decanted in the sodium hexametaphosphate (NaHMP, dispersant)-water (deionized, 18.2 MΩ•cm) mixture for 24 h. Clay-size fractions (0.1–1 μm) were recovered based on Stokes' law (Reinholdt et al., 2013). Then NaHMP-extracted clay slurries were introduced to acid-cleaned centrifuge tubes using a pipette and treated with centrifugation at 10,000 rpm for 0.5 h, and the supernatants were discarded. A 0.5 M NaCl solution was then added into clay slurries, centrifuged at 10,000 rpm for 0.5 h, and the supernatants were discarded. After that, deionized water was added, centrifuged at 10,000 rpm for 0.5 h. This cleaning process with deionized water was repeated to eliminate surface salts until dissolved concentrations of Na and P below the detection limit of Q-ICP-MS (Agilent™ 7900) at sub-ppb levels to ensure that no labile impurities affect K adsorption and solute chemistry.

Prior to adsorption experiments, we examined the possible interference of K released from clay structures based on the control group (a solid-to-liquid ratio of 10 $g{\cdot}L^{-1}$) in which no considerable exogenous K was introduced (Fig. S1). To ensure experimental accuracy, the final release from clays in the control group was found to be less than 0.5 $ng{\cdot}g^{-1}$ K, far less than the K loading (over two orders of magnitude difference). Therefore, even if the partial release of clay K occurs in the initial stage of reaction due to slight dissolution of aluminosilicates, we could infer that this contribution should be negligible, considering slight dissolution detected at the end of experiments. It was thus assumed that K loss from initial fluids during the experiments was due to its adsorption onto clays. Clay minerals obtained in wet conditions were heated at 60 °C until dryness. The BET-N_2 specific surface areas of kaolinite (KGa-2, 20.14 $m^2{\cdot}g^{-1}$) and smectite (SWy-2, 28.60 $m^2{\cdot}g^{-1}$) were reported in Brazier et al. (2019) and were used in this study to calculate clay K coverage. We produced deionized water (18.2 MΩ·cm) using a Milli-Q system (Direct-Q™ 3UV) for experiment groups and applied ultrapure-grade (>99.99% purity) KCl and NaHMP salts for all experiment groups to avoid potential contamination.

As for clay K adsorption experiments, a 100 mM KCl stock solution has been prepared using dissolving KCl hydrate (Acros Organic™, purity >99.99%) with deionized water (18.2 MΩ·cm). Using this stock solution, solutions of lower K concentrations (0.005–20 mM) at circumneutral pH were made. The ionic strength (IS) of fluids was adjusted by optima-grade NaCl (background electrolyte). Commercially purchased hydrochloric acid (HCl, ACS-grade) was further purified in-house by double-distillation using the Teflon® sub-boiling still and then diluted to required molarities with deionized water. All solutions were freshly prepared prior to experiments and uniformly added into clay suspensions. Labwares have been carefully cleaned in a clean hood following an established method. This method uses diluted optima-grade (HCl + HNO_3) and deionized water. Labwares were stored in a laminar flow hood (Airclean™) before usage.

2.2. Experiment design

In brief, we designed several sets of experiments, similar to those described previously (Li and Liu, 2020). To examine the impacts of common environment factors on the K isotopicfractionation between fluids and solids, three individual experiment sets were conducted in ambient conditions:

(1) Time-series experiments, in which we tracked aqueous chemistry as a function of reaction time for up to 15 days, with a constant starting KCl concentration ([K] of 0.2 mM), solute pH of 8, and solute IS of 0.001 M (sorption experiments were performed using 10 $g{\cdot}L^{-1}$ kaolinite and 2 $g{\cdot}L^{-1}$ smectite, respectively). The time-series experiments were designed to provide temporal changes in K adsorption and the time long enough to achieve the equilibria. (2) pH-dependent experiments, in which we modulated solute pH from 4 to 10 (±0.2), with initial [K] of 0.2 mM and solute IS of 0.001 M and 0.1 M for 15 days (10 $g{\cdot}L^{-1}$ kaolinite and 2 $g{\cdot}L^{-1}$ smectite). The pH-dependent experiments were designed to estimate pH influence on K adsorption during the protonation and deprotonation of binding sites. (3) Concentration-control experiments in which we varied initial [K] ranging from 0.005 to 1 mM for kaolinite and 0.2 to 20 mM for smectite), with IS from 0.001 to 0.5 M and solute pH of 8 for 15 days. The concentration-control experiments were designed to have different amounts of initial KCl with a constant solid-to-fluid ratio (10 $g{\cdot}L^{-1}$) to provide a range of percentages of clay K adsorption. The tests using highly concentrated KCl solutions for smectite aimed to probe into both external surface and interlayer space. In experiment sets, the choices for [K], IS, and pH were made based on natural environments. For example, the addition of 0.5 M IS in experiment set (3) aimed to investigate the pattern of K adsorption and associated K isotopic fractionations in high salinity aqueous environments (e.g., seawater, brines, and some types of groundwater, Miller et al., 1986).

Each experimental group consisted of a series of individual batch experiments so that both solids and fluids could be collected and measured in all experimental conditions. All batch experiments were performed in 50 mL centrifuge tubes (acid pre-cleaned, kept sealed) filled with clay slurries under ambient conditions and continuously stirred at 150 rpm in a thermostatic water bath shaker (Thermo Scientific™). The starting solutions used in the experiment have been pre-equilibrated with clay suspensions. In addition, we varied the background electrolyte (NaCl) to investigate the effect of IS on surface complexation (chemisorption vs. physisorption) due to cation competi-

tion (K^+ vs. Na^+) for limited surface sites without direct bonding (i.e., outer-sphere complexation, Guinoiseau et al., 2016). The total experiment duration was set up to 15 days, which should be long enough to reach the adsorption and isotope equilibria and short enough to avoid clay dissolution (Guinoiseau et al., 2016). This approach can be further supported by the results of our time-series experiments. Clay adsorption normally generates slight pH variations at the start of the reaction (Brazier et al., 2019) because of the amount of H^+ exchanges with cations at clay surfaces. Solute pH was monitored and adjusted every six hours using diluted NaOH and HCl solutions (small volumes, negligible compared with initial IS) for the individual reaction in each tube over the course of the experiment (15d). The analytical uncertainty of solute pH is ± 0.1, and fluctuation in solute pH was confirmed to be within ± 0.25 of intended values.

To achieve a sufficient separation of dissolved and adsorbed K fractions, clay suspensions were centrifuged, and the SUPERNATANTS were recovered using syringe filtration at < 0.2 μm at the end of experiments (cellulose acetate). Filtrates were acidified using HCl and then stored at 4 °C. A small aliquot of the experimental solutions was used to determine the distribution of K between solutions and adsorbed phase. We note that the filtration process did not modify aqueous K concentration more than 3% (within the analytical uncertainty), and $\delta^{41}K$ value of filtered standard solution used in this study was identical to the $\delta^{41}K$ of commercial KCl salt (0.20 ± 0.06‰). Decanted clays were rinsed with pH adjusted, deionized water to exclude surface droplets until [K] in leachates below the detection limit of the Q-ICP-MS (>1 ppb K).

3. ANALYTICAL METHODS

3.1. pH, element, electrophoretic and mineralogical analyses

As for all the experiments, pH buffers were avoided to minimize undesired complexation and particle aggregation. Solute pH was measured using a portable pH meter (Thermo Scientific™, Orion Star A221). Both solids and reference materials (BHVO-2) were digested in a mixture of concentrated HCl-HNO_3-HF acids at 150 °C, following the approach reported in Li et al. (2019). Filtrates were dried at 100 °C and re-dissolved in 2wt.% HNO_3 for elemental concentration analysis. The concentrations of Li, Na, K, Mg, Al, Fe, Ca, Sr, and Ti were measured using the quadrupole inductively coupled plasma mass spectrometry (Q-ICP-MS, Agilent™ 7900) at the Plasma Mass Spectrometry Lab, the University of North Carolina at Chapel Hill (UNC-CH). The instrument was calibrated using a range of ICP standard solutions of known concentrations. Internal standards, including Be, Ge, Rh, In, Ir, and Bi, were added for instrument drift correction. During Q-ICP-MS analysis, precision of less than 3% (relative standard derivation, RSD) was routinely achieved. The RSD values were calculated based on an average of three individual analysis of the same sample. Three international standards – a basalt standard BHVO-2, a seawater standard NASS-7, and a river water standard SLRS-5 (elemental compositions certified by the United States Geological Survey and the National Research Council of Canada) were measured to evaluate the accuracy and reproducibility of our elemental analysis (Table S1). These measurements yielded an accuracy of less than 10% for reported elements relative to certified values of references. The reference data were compiled and reported in Table S1.

Electrophoretic mobility was measured using a Zetasizer Nano (Malvern™ ZS90) in ambient conditions and was converted to zeta (ζ) potentials using the Helmholtz-Smoluchowski equation using the Zetasizer software. Zeta (ζ) potential data were reported here to quantitatively describe the electrochemical property of clay particles, which can be easily compared to reported data of the same clay in literature. The ζ potentials of clay suspensions with solute IS of 0.001–0.5 M at a pH range of 4–10 were measured (Table S2). Clay suspensions were dispersed in an ultrasonic bath for 5 min and transferred into capillary cells to measure clay surface charges in different experimental settings (Fig. S2). Averaged values (with derivations) were provided from the performance of triplicates prepared, and each was subjected to 20 light scattering measurements to generate enough dataset for statistical analyses. To determine the clay mineralogy and newly formed phases (if any), X-ray diffractograms (XRD) were collected on a Rigaku™ Miniflex II XRD diffractometer with a Cu K_α source over a 2θ range from 20° to 80°. The X-ray beam was operated at 40 kV (voltage) and 40 mA (current), with a step size of 0.3° and a step rate of $3°\cdot min^{-1}$. The X-ray diffractograms of kaolinite and smectite (both reacted and pristine) and KCl salt (solid) were measured (Fig. S3).

3.2. K *K*-edge XANES analysis

The X-ray absorption near edge structure (XANES) is a synchrotron-based technique that can provide information on the speciation of specific elements such as K. The XANES analysis consists of measuring the photon energy spectrum resulting from focusing an X-ray beam to excite 1 s electron to higher energy unoccupied p-state (Berry and O'Neill, 2004). When the primary beam exceeds the binding energy of the 1 s shell electron of the atoms of interest, the absorption spectrum is stepwise increased, which is referred as the "*K*-edge". In this study, two kinds of K structure information at an atomic/molecular scale were obtained from K XANES spectra (i.e., K speciation and K-O coordination number) (Li et al., 2020b). The *K*-edge XANES spectra for reacted clay samples and model references (pristine clays and KCl salt) were collected from the Soft X-ray Micro-Characterization beamline (SXRMB, 06B1-1) at Canadian Light Source (CLS, Saskatoon, Canada). Spectra collection of both pristine clays and reacted clays were designed to decipher the variations in atomic coordination among lattice K, sorbed K, and ionic K in water and to understand isotopic fractionation linked with atomic coordination changes.

This beamline has Si drift fluorescence detector and monochromated with diffraction from the InSb (111) and Si (111) double-crystals, covering a wide energy range from 1.7 to 10.0 keV. After grinding through a 100-mesh

(0.15 mm) sieve, powdered samples were spread as a thin film on double-sided K-free carbon tape adhered onto a copper stick and then placed in a vacuum chamber to reduce beam attenuation. The radiation damage effect was negligible because of satisfactory reproducibility. K *K*-edge XANES spectra were obtained in a partial fluorescence yield mode by the 7-element fluorescence detector with a dwell time of 4.0 s, and the KCl spectrum was collected using a total electron yield mode to avoid self-absorption effects. Over a photon energy range of K *K*-edge (3550–3700 eV), the photon flux is 2×10^{10} photon s^{-1} at 100 mA, and a beam size at the target is ~7 mm × 1 mm (Y. Hu et al., 2010).

Two-step scans were set up for analysis: region I (3568.0–3708.0 eV, a step-size of 0.2 eV) and region II (3648.0–3708.0 eV, a step-size of 1.5 eV). Radiation damage should be negligible, according to the good reproducibility at the same spot and repetitive scans at different spots in the same sample. To improve the signal-to-noise ratio, five to six spectra were averaged and processed in Athena software (Ravel and Newville, 2005). The linear combination fitting (LCF) was attempted for binary combinations. An R-factor was used to estimate the goodness-of-fit, and significance between the fits was evaluated using the Hamilton test ($p < 0.05$) (Calvin, 2013). The number of independent data calculated was normalized to a sum of 100% and determined as the data range divided by the core-hole lifetime broadening. Fits were accepted when the sum of the references' contribution was 100 ± 10% (Fig. 1a). The uncertainty of XANES-LCF is difficult to quantify; as a rule of thumb, the absolute error is ~5–10% (Gu et al., 2019). The extended X-ray absorption fine structure (EXAFS) approaches could offer detailed information on the coordination environment of K. However, this approach was not applicable in this study due to poor signal-to-noise ratios likely caused by the limitation of tender X-ray and very low K concentrations in our samples. We note that both unreacted and reacted clays have been measured for the K *K*-edge XANES, and the spectra of unreacted clays only reflect the feature of K within clay lattice (0.065% K_2O in KGa-2 and 0.53% K_2O in SWy-2, Source Clay Physical/Chemical Data, CMS) and the spectra of reacted clays provide a sum of spectra containing both lattice K and sorbed K that were then treated with the XANES-LCF analysis.

3.3. K Isotope analysis

All chemical pretreatments were performed in the class-100 vented laminar flow workstation (Airclean™, 600 PCR) in the Plasma Mass Spectrometry Lab at the University of North Carolina at Chapel Hill (UNC-CH). An aliquot of digested sample was evaporated to dryness and re-fluxed with 2 mL 0.7 M HNO_3 before loading onto the columns. Potassium isotopic ratio was measured after column purification, following a two-step purification approach reported in Chen et al. (2019). The first column was filled with 17 mL AG50-X8 cation-exchange resin (200–400 mesh, Bio-Rad™) and conditioned using 0.7 M HNO_3. Eluted K fractions were then collected after most of the matrix elements being eluted. Then collected elution was evaporated until dryness on a hotplate >120 °C and re-dissolved in 1 mL 0.5 M HNO_3 for the second column. The second column was filled with 2.4 mL AG50-X8 cation-exchange resin (200–400 mesh, Bio-Rad™) and conditioned in 0.5 M HNO_3. The K fraction was collected after the rest matrix elements being eluted. After chromatographic processes, pre-cuts and post-cuts were measured for K, Na, Al, Fe, Rb, and Ti concentrations on the Agilent™ 7900 Q-ICP-MS. The K collection was ~100% yield to exclude any isotopic fractionations during ion-exchange chromatography. The weight percentage of the sum of other matrix elements to K was checked to ensure a sum of matrix elements below 2% of total K to minimize matrix influences on isotope analysis (Chen et al., 2019). Column blanks were >3 orders of magnitude lower than K amounts in the samples.

Procedural K blanks were periodically monitored for experimental runs (≤10 ng K), which were negligible in comparison to collected K fractions of natural and laboratory samples at μg-/mg-levels. Purified K solutions were introduced into the Nu Plasma II high-resolution MC-ICP-MS at the Isotope Laboratory at the University of Washington, Seattle. The K isotopic ratio analyses were performed using the "cold plasma" mode (low R.F. power from 750 to 850 W) with an Aridus II desolvation system and equipped with a Savillex™ PFA spray chamber and a C-Flow PFA microconcentric nebulizer. To correct instrumentals bias, the K isotopic ratios were measured using a sample-standard bracketing technique using reference NIST SRM 3141a (6–8 analytical cycles for each sample). Instrumentation and analytical details were summarized in Hu et al. (2018). The isotopic composition was expressed in ‰, relative to NIST SRM 3141a (Eq. (1)):

$$\delta^{41}K_{sample}(‰) = \left\{ \frac{(^{41}K/^{39}K)_{sample}}{(^{41}K/^{39}K)_{NIST\ SRM\ 3141a}} - 1 \right\} \times 1000 \quad (1)$$

The long-term reproducibility from replicate analyses of a suite of international references was better than 0.06‰ (95% confidential interval) (Hu et al., 2018; Xu et al., 2019). The granite (GSP-2) and basalt (BHVO-2) USGS standards measured along with samples and measured values fall within the uncertainties of reported data (Table S3). Additionally, clay mineral lattices contain non-negligible amounts of K compared with total amounts of K sorbed, as specified in certificates (https://www.agry.purdue.edu/cjohnston/sourceclays/chem.htm). Measured $\delta^{41}K_{solid}$ data were corrected by the deduction from primary structural K composition of unreacted clays (i.e., pristine clay minerals, $\delta^{41}K_{kaolinite,\ KGa\text{-}2} = -0.44 \pm 0.05‰$ and $\delta^{41}K_{smectite,\ SWy\text{-}2} = -0.63 \pm 0.05‰$, Table S3) following Eq. (2) to calculate the isotopic compositions of adsorbed K on reacted clays:

$$\delta^{41}K_{ad} = \frac{[K]_{solid} \times \delta^{41}K_{solid} - [K]_{pristine\ clay} \times \delta^{41}K_{pristine\ clay}}{[K]_{ad}} \quad (2)$$

where $[K]_{solid}$ and $\delta^{41}K_{solid}$ represent the K concentrations and its isotopic compositions of reacted clays, respectively,

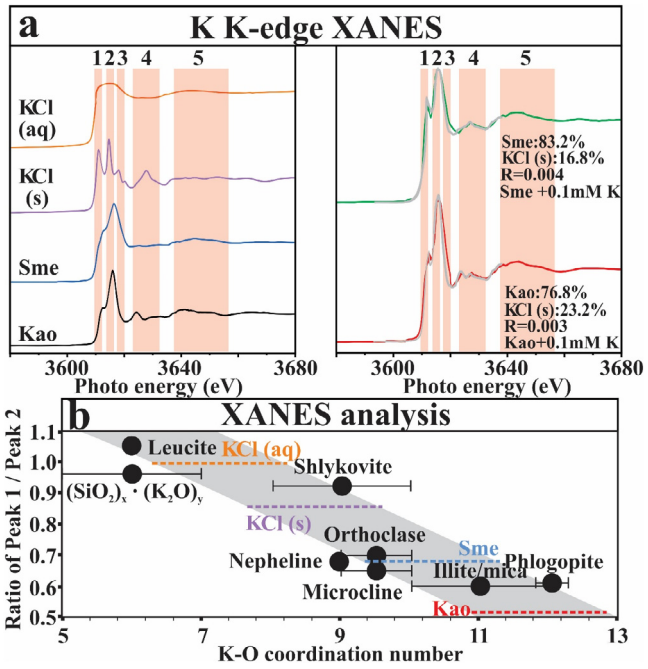

Fig. 1. K XANES spectra of clays before and after reaction. (a) XANES data and linear combination fitting analysis (grey lines as LCF fittings); (b) Intensity ratios between XANES Peak 1 and Peak 2 as a function of atomic K-O coordination number. Peaks 1–5 in the plot (a) reflect a result of the dipole transition of a *1s* electron to unoccupied *4p* orbital, with a small contribution of quadrupole transitions to *3d* orbitals, which could offer the coordination information. The result of XANES-LCF in the plot (a) is highlighted by grey lines, which indicates that clay surface outer-sphere K^+ became KCl (s) during the drying of clays after experiments (reacted clays have been rinsed using deionized water until K in eluents below the Q-ICP-MS detection limits). Relative contributions of each K speciation are provided based on the best least square fit ranked after an R-factor as the goodness of fitting. In the plot (b), data of leucite, orthoclase, K-bearing silicates, microcline, phlogopite, nepheline, shlykovite, and illite/mica are from literatures (Huffman et al., 1986; Spiro et al., 1986; Greaves et al., 1991; Kamijo et al., 1996; Cibin et al., 2005; Glezakou et al., 2006; Xu et al., 2011; Roberts et al., 2018; Geng et al., 2020). The grey area demonstrates an eye-guiding trend and dashed lines show visual estimation of clays (Kao: kaolinite; Sme: semctite).

and $[K]_{clay}$ and $\delta^{41}K_{clay}$ denote the K concentrations and isotopic compositions of pristine clays, respectively. We suggest that the removal of K from the starting solution was solely caused by K adsorption on clays and that unreacted clay surfaces were K-free after cleaning. In addition, the isotopic compositions of adsorbed K could be calculated based on mass balance (Eq. (3)), using $\delta^{41}K_{aq}$ dtat and the percentage of K adsorption (F, %). The same method was adopted in early studies (Ge: Yuan et al., 2018; Cu & Zn: Balistrieri et al., 2008; W: Wasylenki et al., 2020).

$$\delta^{41}K_{ad} = [100 \times \delta^{41}K_{KCl} - (100 - F) \times \delta^{41}K_{aq}]/F \quad (3)$$

Since K loss during sampling cannot be prevented, we compared the total amount of K addition in each experiment to a sum of the amount recovered in fluid and solid phases (Wasylenki et al., 2020) to confirm K recovery and validity of experimental results. Measured $\delta^{41}K_{ad}$ values are comparable to calculated $\delta^{41}K_{ad}$ based on the mass balance approach (Table 1), and the isotopic offset between two values is less than analytical uncertainties by the following equation (Eq. (4)):

$$[\delta^{41}K_{KCl} - (\delta^{41}K_{aq} \times (100 - \%ad) + (\text{measured } \delta^{41}K_{ad} \times \%ad)]/2 \leq 0.06‰(95\%\text{c.i.}) \quad (4)$$

Isotope mass balance calculation confirms that an abundance-weighted sum of isotopic values for aqueous K and adsorbed K was within the uncertainty of KCl (i.e., a sum of parts equals the whole). Net isotopic fractionation between adsorbed and aqueous K, $\Delta^{41}K$ is defined as (Eq. (5)):

$$\Delta^{41}K_{ad-aq} = \delta^{41}K_{ad} - \delta^{41}K_{aq} \quad (5)$$

Two standard deviations (2 S.D.) and 95% confidential interval (95% c.i.) were calculated using 4–8 repeated runs within the same analytical sessions. We calculated 95% c.i. using Eq. (6):

$$95\%\text{c.i.}(‰) = t_{n-1} \times \frac{S.D.}{\sqrt{n}} \quad (6)$$

where SD notates the standard deviation over the analytical sessions (times = n) of the sample, and t_{n-1} is the student's law factor with n − 1 degrees of freedom at a 95% confidence level. The estimated uncertainties on net fractionation $\Delta^{41}K_{ad-aq}$ were propagated using Eq. (7):

$$\Delta E = \sqrt{(c_1\Delta W_1)^2 + (c_2\Delta W_2)^2 + \cdots + (c_n\Delta W_n)^2} \quad (7)$$

where ΔE is an absolute error, c is a multiplicative factor, and W is additive function inputs.

Table 1
Experimental setup and data of K adsorption on clay minerals and isotopic fractionation in time-series, pH-dependent and concentration control sets for referenced kaolinite and smectite.

Syst.	No.	Time	pH	$[K]_{Initial}$	Adsorption	$[K]_{ad}$	$\delta^{41}K_{aq}$	95%c.i.	$^{1}\delta^{41}K_{ad}$	$^{2}\delta^{41}K_{ad}$	$^{3}\delta^{41}K_{ad}$
		h		mM	%	$\mu M/m^3$	‰	‰	‰	‰	‰
Time-series set	10 g/L Kaolinite	0.25	8	0.2	63.4	0.63	−0.14	0.04	0.40	n.d.	n.d.
	IS = 0.001 M	1			72.3	0.72	−0.24	0.04	0.37		
		3			71.1	0.71	n.d.	n.d.	n.d.		
		12			72.0	0.71	−0.36	0.04	0.42		
		24			74.7	0.74	n.d.	n.d.	n.d.		
		72			74.2	0.74	−0.35	0.04	0.39		
		168			77.1	0.77	n.d.	n.d.	n.d.		
		360			72.3	0.72	−0.32	0.04	0.40		
	2 g/L Smectite	0.25	8	0.2	30.0	1.40	0.05	0.05	0.55	n.d.	n.d.
	IS = 0.001 M	1			42.3	1.48	−0.04	0.04	0.53		
		3			52.5	1.84	n.d.	n.d.	n.d.		
		12			54.6	1.91	−0.25	0.04	0.57		
		24			60.6	2.12	n.d.	n.d.	n.d.		
		72			56.3	1.97	−0.22	0.05	0.53		
		168			58.3	2.04	n.d.	n.d.	n.d.		
		360			54.5	1.91	−0.22	0.05	0.55		
pH-dependent set	10 g/L Kaolinite	360	4	0.2	13.2	0.13	0.10	0.04	0.86	0.90	−0.24
	IS = 0.001 M		6		51.1	0.51	−0.18	0.04	0.56	n.d.	n.d.
			8		73.7	0.73	−0.35	0.04	0.40	n.d.	n.d.
			10		80.0	0.79	−0.43	0.04	0.36	0.38	−0.03
	10 g/L Kaolinite	360	4	0.2	8.1	0.08	n.d.	n.d.	n.d.	n.d.	n.d.
	IS = 0.1 M		6		15.1	0.15					
			8		18.2	0.18					
			10		17.1	0.17					
	2 g/L Smectite	360	4	0.2	31.1	1.09	−0.03	0.04	0.71	0.68	−0.37
	IS = 0.001 M		6		41.6	1.45	−0.12	0.05	0.65	n.d.	n.d.
			8		55.7	1.95	−0.23	0.05	0.54	n.d.	n.d.
			10		57.4	2.01	−0.24	0.05	0.53	0.50	−0.28
	2 g/L Smectite	360	4	0.2	9.3	0.33	n.d.	n.d.	n.d.	n.d.	n.d.
	IS = 0.1 M		6		8.4	0.29					
			8		11.9	0.42					
			10		10.8	0.38					

Table 1
Continued

Syst.	No.	Time	pH	$[K]_{Initial}$	Adsorption	$[K]_{ad}$	$\delta^{41}K_{aq}$	95%c.i.	$^{1}\delta^{41}K_{ad}$	$^{2}\delta^{41}K_{ad}$	$^{3}\delta^{41}K_{ad}$
		h		mM	%	$\mu M/m^3$	‰	‰	‰	‰	‰
Concentration-control set	10 g/L Kaolinite IS = 0.001 M	360	8	1	24.9	1.24	0.03	0.04	0.71	n.d.	n.d.
				0.5	47.4	1.18	−0.13	0.05	0.57		
				0.2	74.6	0.74	−0.35	0.04	0.39		
				0.1	71.4	0.35	−0.31	0.05	0.40		
				0.05	76.3	0.19	−0.41	0.04	0.39		
				0.03	81.7	0.12	−0.43	0.04	0.34		
				0.015	84.3	0.06	−0.47	0.04	0.32		
				0.005	92.7	0.02	−0.53	0.04	0.26		
	10 g/L Kaolinite IS = 0.1 M	360	8	1	22.0	0.60	n.d.	n.d.	0.80	n.d.	n.d.
				0.5	18.8	0.47	0.07	0.05	0.76		
				0.2	18.0	0.18	0.06	0.05	0.84		
				0.1	14.4	0.07	0.10	0.05	0.79		
				0.05	9.4	0.02	0.13	0.04	0.87		
				0.03	2.0	0.00	0.19	0.04	0.84		
				0.015	2.0	0.00	n.d.	n.d.	0.89		
	10 g/L Kaolinite IS = 0.5 M	360	8	1	3.4	0.17	n.d.	n.d.	n.d.	n.d.	n.d.
				0.5	1.7	0.04					
				0.2	1.8	0.02					
				0.1	3.1	0.02					
				0.05	2.7	0.01					
		360	8	20	1.8	6.29	n.d.	n.d.	n.d.	n.d.	n.d.
	2 g/L Smectite			10	1.9	4.98					
	IS = 0.001 M			5	3.1	4.11					
				2	9.3	3.25					
				1	15.7	2.74					
				0.5	35.2	3.05					
				0.2	55.7	1.95					
	2 g/L Smectite	360	8	20	0.2	2.85	n.d.	n.d.	n.d.	n.d.	n.d.
	IS = 0.1 M			10	0.8	2.33					
				5	1.5	1.84					
				2	3.9	1.36					
				1	4.4	0.77					
				0.5	4.8	0.42					
				0.2	11.9	0.42					
	2 g/L Smectite	360	8	20	0.1	1.08	n.d.	n.d.	n.d.	n.d.	n.d.
	IS = 0.5 M			10	0.3	0.69					
				5	0.5	0.65					
				2	0.9	0.34					
				1	0.9	0.16					
				0.5	1.1	0.10					
				0.2	1.9	0.07					

Note 1: IS: ionic strength (NaCl); n.d. means not determined. 95% c.i. = 95% confidence interval, notates the two standard error corrected by the Student's t factor.
Note 2: [1]calcuated $\delta^{41}K_{ad}$ based on mass balances; [2]measured $\delta^{41}K_{ad}$ after calibration; [2]measured $\delta^{41}K_{solid}$.

4. RESULTS

4.1. Characterization of reacted clays

The data of ζ potential measurement are summarized in Table S2 and provided in Fig. S2. As pH increased from 4 to 10, the ζ potentials of kaolinite and smectite suspensions decreased, ranging from -42 ± 2 to -19 ± 2 eV and from -22 ± 1 to -49 ± 2 eV, respectively. Under the same experimental condition, smectite showed slightly higher densities of negative charge than kaolinite. Ionic strength appears to have no impact on the ζ potential of clays.

The results of two kinds of X-ray analyses (XRD and K XANES) are shown in Fig. 1a and S3. There was no modification in clay mineralogy after dryness before and after the experiments. However, the characteristic peaks (I and II, Fig. 1a) of KCl in solid phases appeared in the X-ray diffractogram of reacted kaolinite and smectite, which were further examined by the K *K*-edge XANES spectra. Based on the comparison of XANES spectra features (peak positions and shapes) between unreacted clays and references, major absorption resonances (Peaks 2 and 3) can be observed within the energy range of 3605–3620 eV, along with the shoulder on the pre-edge peaks (Peak 1) at the rising part of spectra. Minor Peaks 4 and 5 can be found in the after-edge regions, reflecting the crystallinity. Changes in spectral features (e.g., peak intensity and energy shifts) of peaks (1–5, Fig. 1a) suggested the appearance of KCl (s) on clays after reacting with 0.1 mM [K]. Considering negligible K in leachates by pre-cleaning, the KCl presence in reacted clays is likely from solid dryness after the experiments, rather than surface excess salts. Therefore, the results from the XANES-LCF indicated that the percentage of adsorbed K in the total K pool of clays (a sum of adsorbed K on clay surfaces and primary K in clay lattices) was $23.2 \pm 2.4\%$ and $16.8 \pm 2.1\%$, in reacted kaolinite and smectite, respectively.

4.2. Characterization of K adsorption patterns

Clay adsorption results are summarized in Table 1 and shown in Figs. 2–5.

In time-series experiments (pH of 8 and IS of 0.001 M), the percentages of K adsorbed onto clays range from 63.4 to 77.1% (kaolinite) and from 30.0 to 60.6% (smectite), respectively. A rapid increase in the percentage of K adsorption onto clays existed during the early stage of reaction (stage I, <12 h) and it rapidly reached the equilibrium at the end of experiments (stage II) (Fig. 2). Hence, clay K coverage (adsorbed K content divided by clay BET-N_2 surface area) was ~0.7 μmol $K \cdot m^{-2}$ (kaolinite) and ~2.0 μmol $K \cdot m^{-2}$ (smectite), respectively (Fig. 5).

In pH-dependent experiments, the percentage of K adsorbed on clays increased from 13.2 to 80.0% (kaolinite) and 31.1 to 57.4% (smectite), respectively, with solute pH increasing from 4 to 10 (low IS of 0.001 M). At high IS of 0.1 M, the percentage of K adsorption decreased to ranges from 8.1 to 17.1% (10 $g \cdot L^{-1}$ kaolinite) and 8.4 to 11.9% (2 $g \cdot L^{-1}$ smectite) (Fig. 3). Clay K coverage was 0.1–0.8 μmol $K \cdot m^{-2}$ (kaolinite) and 1.1–2.0 μmol $K \cdot m^{-2}$ (smectite) at low IS, and 0.1–0.2 μmol $K \cdot m^{-2}$ (kaolinite) and 0.4–0.6 μmol $K \cdot m^{-2}$ (smectite) at high IS (Fig. 5).

In concentration-control experiments (pH of 8), the percentage of K adsorbed onto clays decreased with incremental [K] from 0.005 to 1 mM, ranging from 24.9 to 92.7% for kaolinite (low IS of 0.001 M). Kaolinite K adsorption ratio decreased to 2.0–22.0% (high IS of 0.1 M) and 1.7–3.4% (high IS of 0.5 M). Kaolinite K coverage increased from near zero to a plateau at ~1.0 μmol K/m^2, when initial [K] increased from 0.005 to 1 mM, and clay K coverage reached ~0 as IS increases. Clay K adsorption ratio decreased with incremental [K] from 0.2 to 20 mM at IS of 0.001 M, ranging from 1.9 to 55.7% for smectite. Smectite K adsorption ratio decreased to 0.2–11.9% (high IS of 0.1 M) and 0.1–1.9% (high IS of 0.5 M) (Fig. 4). Smectite K coverage increased from ~2.0 μmol $K \cdot m^{-2}$ to ~6.0 μmol $K \cdot m^{-2}$, when starting [K] increased from 0.2 to 20 mM (low

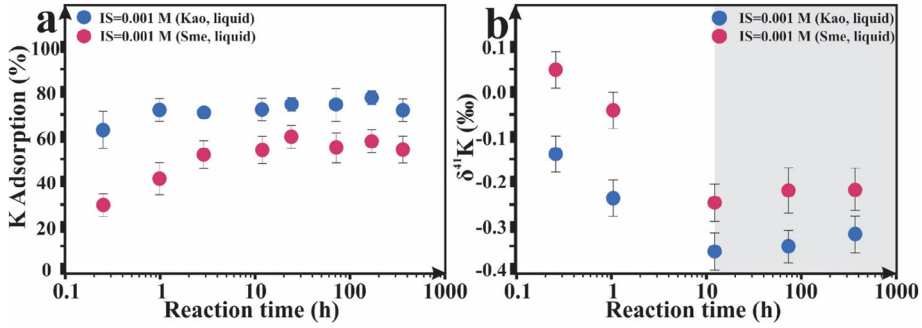

Fig. 2. Illustration of K elemental and isotopic patterns in time-series experiments with 0.2 mM [K] at pH = 8 and IS = 0.001 M. (a) The K adsorption ratios during clay surface exchange at reaction time ranging from 0.25 to 360 h; (b) Temporal change in K isotopic composition in aqueous phases during clay surface exchange at the reaction time ranging from 0.25 to 360 h. Dissolved phases (filtered) were analyzed for K isotopic composition. In the plot (b), the isotope stages I (white area) and II (grey area) reveal that initial kinetic fractionation (preferential ^{39}K diffusion) and close-to-equilibration status. Error bars on the Y-axis show (a) the 2 S.D. of the adsorption experiment triplicates, and (b) the analytical uncertainties of isotopic measurements using a MC-ICP-MS at the U.W. - Seattle. Abbreviations: Kao: kaolinite; Sme: smectite; IS: ionic strength (background electrolyte by NaCl).

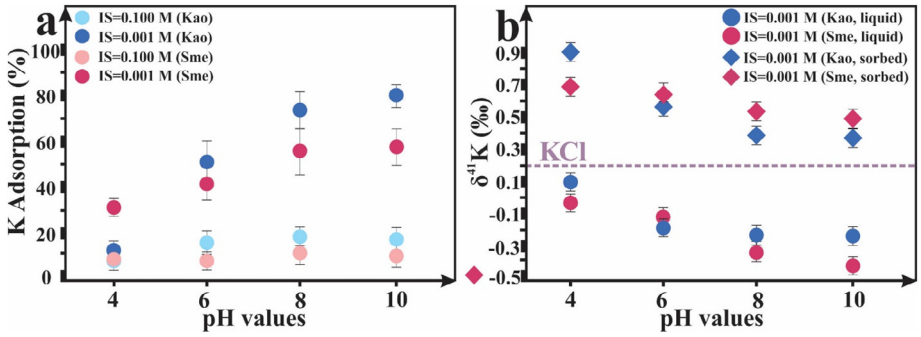

Fig. 3. Illustration of K elemental and isotopic patterns in pH-dependent sets with 0.2 mM [K] at IS of 0.001 M and 0.1 M, respectively, over a wide pH range from 4 to 10 after 15-d reaction. (a) The adsorption ratio of K during clay surface exchange; (b) The K isotopic composition of aqueous and sorbed phases during clay surface exchange. Please note that only $\delta^{41}K_{ad}$ data based on mass-balance calculation are plotted, and measured $\delta^{41}K_{ad}$ values are summarized in Table 1. Both dissolved (filtered) and adsorbed phases were measured for K isotope ratios. Error bars on the Y-axis are the same as those in Fig. 2. The K isotopic composition of starting KCl solution (dashed purple line) is 0.20 ± 0.04‰. Abbreviations: Kao: kaolinite; Sme: smectite; IS: ionic strength (background electrolyte by NaCl).

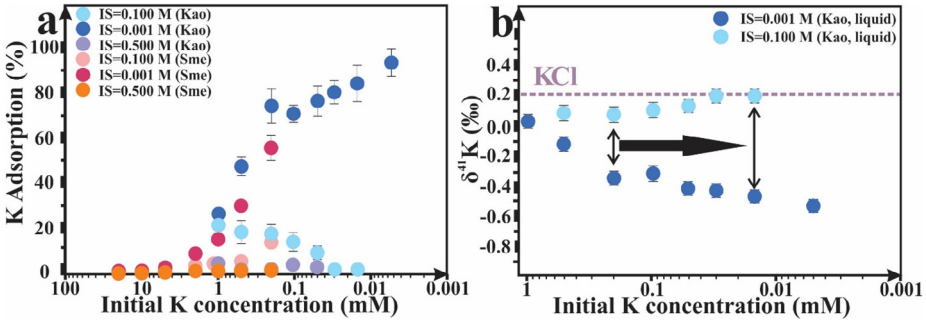

Fig. 4. Illustration of K elemental and isotopic patterns in concentration-dependent sets with 0.005–1 mM [K] for kaolinite and 0.2–20 mM [K] for smectite at pH = 8 and IS of 0.001–0.2 M after 15-d reaction. (a) The absorption ratio during clay surface exchange; (b) The isotopic composition of aqueous K. Only dissolved phases were analyzed for K isotopic composition. Error bars on the Y-axis are the same as those in Figs. 2 and 3. The black arrows in the plot (b) displays the degrees of K isotopic variation between aqueous K (filtered) in kaolinite and smectite sets with changing [K] (or adsorption ratio). K isotopic compositions of dissolved phases in smectite tests were not measured due to low adsorption ratios, and thus limited isotope fractionation. The isotopic value of KCl (dashed purple line) is 0.20 ± 0.04‰. Abbreviations: Kao: kaolinite; Sme: smectite; IS: ionic strength (background electrolyte by NaCl).

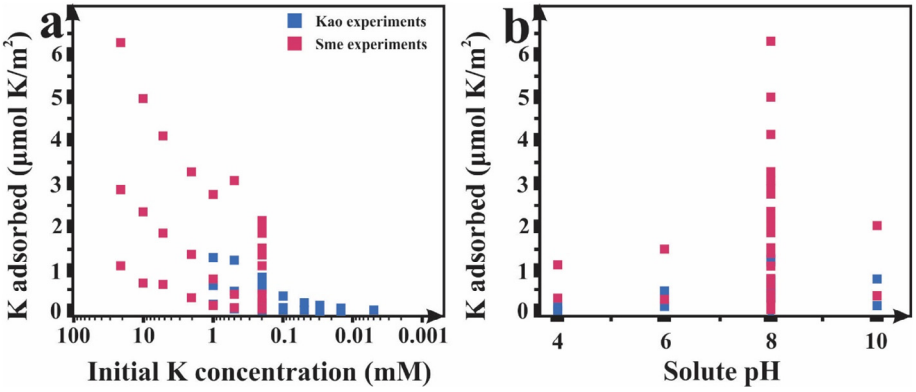

Fig. 5. Clay K coverage as a function of (a) initial [K] and (b) solute pH. Kao: kaolinite; Sme: smectite. Data points are marked by kaolinite (blue) and smectite (red). Clay K coverage was calculated using adsorbed K content divided by the BET-N_2 specific surface areas of kaolinite (KGa-2, 20.14 $m^2 \cdot g^{-1}$) and smectite (SWy-2, 28.69 $m^2 \cdot g^{-1}$), respectively (Brazier et al., 2019).

IS of 0.001 M), and smectite K coverage reached ~0 with IS increasing (Fig. 5).

4.3. Characterization of K isotopic fractionation

The isotopic compositions of aqueous and adsorbed K are provided in Table 1. The K isotopic compositions of the filtrates were measured from experimental solutions, and these of the adsorbed K were calculated based on mass balance (Eq. (3), except for four data points measured in the (2) pH-dependent set). The K isotopic composition of prepared KCl solution was 0.20 ± 0.06‰. The first-order observation is that the heavy K isotope was preferentially sorbed on clays compared with K left in surrounding solutions. Mass balance calculation showed that $\delta^{41}K_{ad}$ values ranged from 0.26‰ to 0.89‰. The net isotopic fractionation $\Delta^{41}K_{ad\text{-}aq}$ values were negative at the incipient stage (<12 h) and became positive as experiments proceed. The net isotopic fractionation $\Delta^{41}K_{ad\text{-}aq}$ ranged from ~0.6 to 0.8‰, despite variations in pH, [K], and clay K coverage (Figs. 2–4 and 7).

In time-series experiments (pH = 8 and IS = 0.001 M), the isotopic composition of aqueous K in solution ranged from −0.14 ± 0.04‰ to −0.36 ± 0.04‰ (kaolinite), and from −0.25 ± 0.04‰ to 0.05 ± 0.05‰ (smectite) (Fig. 2). The isotope equilibria were probably achieved within the first 12-hour because subsequent analyses of the same runs at the end of experiments resulted in near-identical adsorption ratios and $\delta^{41}K_{aq}$ values within the analytical uncertainties.

In pH-dependent experiments (IS = 0.001 M), the isotopic composition of aqueous phases ranged from −0.43 ± 0.04 to 0.10 ± 0.04‰ (kaolinite) and −0.24 ± 0.05 to −0.03 ± 0.04‰ (smectite), respectively (Fig. 3). The $^{41}K_{aq}$ values negatively correlated to the adsorption ratios, consistent with the increase in solute pH in the studied pH range (4 to 10 ± 0.2). Measured isotopic composition of K sorbed onto clays ($\delta^{41}K_{ad}$) ranged from 0.38 ± 0.04 to 0.90 ± 0.04‰ (kaolinite) and 0.50 ± 0.04 to 0.68 ± 0.04‰ (smectite), respectively, in accordance with mass-balance estimation.

In concentration-control experiments (pH = 8 and IS = 0.001 M), the K isotopic composition of aqueous phases varied from −0.53 ± 0.04 to 0.03 ± 0.04‰ (kaolinite) (Fig. 4). No isotope data of smectite in this set were measured due to limited adsorption percent and thus negligible K isotopic fractionation. The isotopic compositions of K left in the solutions (kaolinite) changed to a range of 0.03–0.19‰ at IS of 0.1 M along with the reduction in K adsorption ratio. High IS inhibited K adsorption, but it did not affect the K isotopic fractionation between aqueous and sorbed phases.

To distinguish the equilibrium from kinetic isotopic fractionation mechanism, we describe the K isotopic fractionation between absorbed ($\delta^{41}K_{ad}$) and aqueous K ($\delta^{41}K_{aq}$) using both equilibrium (batch steady-state, see Eq. (8)) and kinetic (modeled as "Rayleigh fractionation", Eq. (9)) models:

$$\delta^{41}K_{ad} = \left(\frac{\alpha \times \delta^{41}K_{KCl} + 1000 f_K \times (\alpha - 1)}{\alpha(1 - f_K) + f_K}\right); \delta^{41}K_{aq} = (\delta^{41}K_{KCl} - f_K)/(1 - f_K) \quad (8)$$

$$\delta^{41}K_{ad} = \left(\frac{(\delta^{41}K_{KCl} + 1000) \times (1 - (1 - f_K) \times \alpha)}{f_K - 1000}\right); \delta^{41}K_{aq} = e^{[(\alpha-1)\ln f_K + \ln(\delta^{41}K_{KCl} + 1000)]} - 1000 \quad (9)$$

where $\alpha_{ad\text{-}aq}$ is the fractionation factor, $\delta^{41}K_{KCl}$ is the $\delta^{41}K$ value of initial KCl (0.20 ± 0.04‰), and f_K denotes the proportion of K left in solutions (i.e., ($1\text{-}f_K$) is the proportion of K adsorbed on clays). The equilibrium model assumes continuous, reversible isotope exchange as the reaction continues in closed systems (Johnson et al., 2004, Fig. 6a). The kinetic model considers that one phase can be continuously

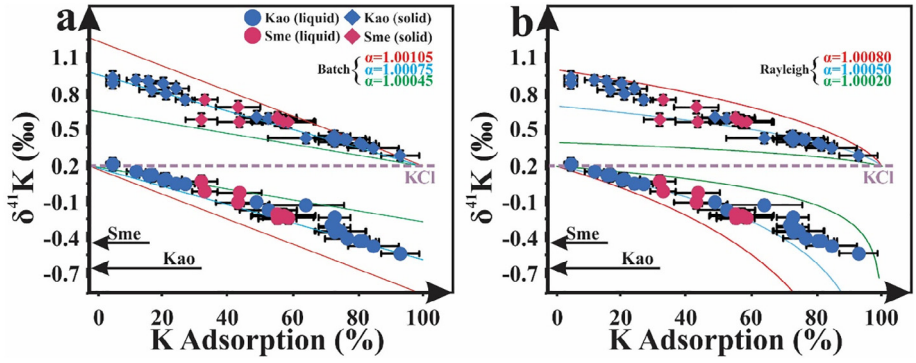

Fig. 6. The K isotopic fractionation plotted against the adsorption percent. (a) Batch model fits of isotopic composition in dissolved and adsorbed K (only using calculated $\delta^{41}K_{ad}$) during adsorption onto clay minerals vs. the percentage of K adsorption; (b) The Rayleigh model fits of K isotopic fractionation in dissolved and adsorbed K (calculated $\delta^{41}K_{ad}$) during adsorption on clay minerals vs. the percentage of K adsorption. Isotope data are described by a best-fit equilibrium path using the fractionation factor $\alpha_{ad\text{-}aq}$ of ~1.00075. Analytical uncertainties are smaller than the symbol sizes. The arrows in the plots (a-b) denote the K isotopic composition of kaolinite (−0.44 ± 0.05‰) and smectite (−0.63 ± 0.05‰). The K isotopic composition of starting KCl solution (dashed purple line) is 0.20 ± 0.04‰. Kao: kaolinite; Sme: smectite. The isotopic composition of adsorbed K was estimated using mass balance calculation.

removed from the system, which is not fully reversible (Fig. 6b). In summary, the equilibrium (batch steady-state) model provides the best fit ($\alpha_{ad\text{-}aq}$ of ~1.00075).

5. DISCUSSION

Our experimental results indicate that K isotopes are substantially fractionated during K adsorption onto clay minerals, probably resulting from the equilibrium isotopic exchange process; heavier K isotopes are preferentially adsorbed onto kaolinite and smectite. Consequently, the K isotopic fractionation factors between aqueous and adsorbed phases remain near-identical ($\Delta^{41}K_{ad\text{-}aq}$ about 0.6–0.8‰), although the isotopic compositions of dissolved and adsorbed K in experiments vary widely from −0.53 to 0.90‰ in various experimental conditions. This feature is explained by variations in adsorption percent following the same isotopic fractionation mechanism. Below, we determine the potential K isotopic fractionation mechanisms during clay adsorption. Then we evaluate the difference in K isotopic fractionation during clay adsorption and incorporation. Broader implications for tracing chemical weathering and climate using geologic K records are presented in the end.

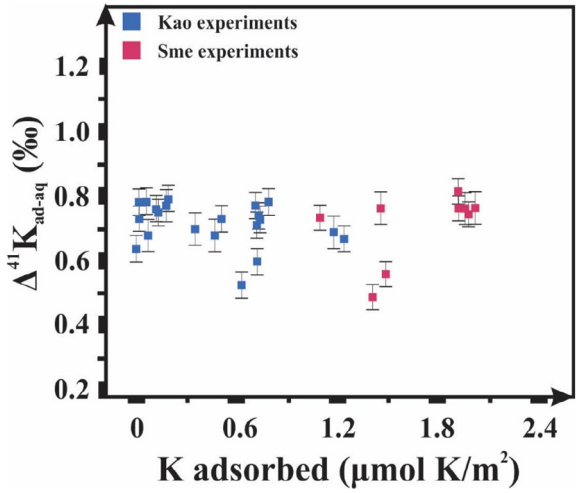

Fig. 7. Illustration of K isotopic fractionation as a function of clay K coverage (μmol K/m^2). Kao: kaolinite; Sme: smectite; Data points are marked by kaolinite (blue) and smectite (red). Clay K coverage was calculated using adsorbed K divided by BET-N_2 specific surface areas clays. The isotopic composition of sorbed K was calculated based on K mass balance, which was alsoused to estimate $\Delta^{41}K_{ad\text{-}aq}$.

5.1. K isotopic fractionation during clay adsorption

5.1.1. Fractionation patterns

In most cases, a short-lived kinetic pattern (transient scatters with heavy K isotopes enriched in solutions) occurs at the initial adsorption stage (Tl, Nielsen et al., 2013; Zn, Dong and Wasylenki, 2016; Ca; Brazier et al., 2019; Se, Xu et al., 2020), and rapidly diminishes when the equilibrium is reached. This kinetic trend is not distinguishable for K isotopes that might be ascribed to the overprint of subsequent isotope equilibrium.

A conceptual scheme depicted for K adsorption and its isotopic fractionation on clays is provided (Fig. 8): (i) a kinetic isotopic fractionation step promoted by diffusion, (ii) an isotopic transition from kinetic to equilibria with gradual contribution of backward reactions, and (iii) eventually an isotope equilibrium status of surface complexation with ions in solutions. Initial diffusion of isotopically lighter K towards clay external surfaces (and the interlayer space of smectite) with restrained backward reactions (Bourg et al., 2010) preferentially enriches heavy K isotopes in solutions. This transient feature may be masked by rapidly established K isotopic equilibria.

The near-constant net isotopic fractionation factors ($\Delta^{41}K_{ad\text{-}aq}$) of ~0.6–0.8‰ shown in Fig. 7 and the parallel linear pattern depicted in Fig. 6 suggest equilibrium K isotoppc fractionation with $\alpha_{ad\text{-}aq}$ of ~1.00075. The parallel trends defined by the K isotopic compositions over various K fractions are indicative of the equilibrium law (rapid,

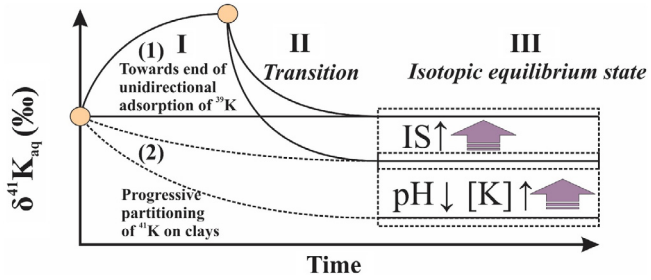

Fig. 8. Conceptual illustration showing temporal K isotope variations in aqueous K, dependent on reaction time, pH, initial concentration ([K]), and ionic strength (IS). In the plot, the path (1) reflects successive K isotopic fractionation during adsorption, including (I) an initial kinetic isotopic fractionation due to preferential diffusion of ^{39}K to clay surfaces/interlayers, (II) gradual transition to isotopic equilibria with surrounding aqueous medium, and (III) an eventual equilibrium isotopic fractionation with preferential ^{41}K adsorption on clays. The path (2) implies gradual establishment of isotopic equilibria without kinetic processes. In the dashed box, isotopic fractionations between aqueous K and initial KCl become smaller with lower degrees of adsorption, as ionic strength (IS) and initial KCl concentration ([K]) are higher, and/or solute pH is lower. Isotopically lighter K is prone to be incorporated into clay structures based on field observations (S. Li et al., 2019; Chen et al., 2020; Santiago Ramo et al., 2020; Teng et al., 2020; Wang et al., 2020b) and heavier K tends to be sorbed on clay surfaces.

continuous isotope exchange between aqueous and sorbed K). Therefore, K isotoppc fractionation is thermodynamically driven, and the forward and backward reactions (adsorption and desorption) are likely reversible.

5.1.2. Mineralogy controls

Next, we investigate whether the K isotopic fractionation factor for kaolinite differs from that of smectite. Despite similarities in K complexation mode (i.e., outer-sphere complexation), we infer that the equilibrium K isotopic fractionation occurring during clay adsorption might be site-dependent (i.e., clay basal surface, edge surface, and/or interlayer space). Specifically, adsorption-driven isotopic fractionation might be closely associated with clay charge density in different sites, as reported in a study of Ca^{2+} adsorption on kaolinite, montmorillonite, and muscovite (Brazier et al., 2019). Only limited isomorphic substitution of tetrahedral Si and/or octahedral Al exist in kaolinite, with pH-dependent charges developing on hydroxyls at edge surface and little pH-independent negative basal charges (Schoonheydt and Johnston, 2006; Au and Leong, 2013). By contrast, considerable permanent negative layer charges present at the interlayer sites of smectite. This is consistent with decreases in ζ potentials of clay suspensions promoted by hydroxyl deprotonation with increments in solute pH, and its decrease with pH in smectite (SWy-2) is less significant relative to kaolinite (KGa-2) (Fig. S2). Such a near-flat ζ-pH pattern of smectite is less obvious in collected ζ data in this study relative to other ζ data in the literature, but it is acceptable considering uncertainties (i.e., zeta derivation).

Nevertheless, their isotopic patterns were similar, and our data cannot tell the difference in the K isotopic fractionation factors between these two clays (Fig. 6). To reach the interlayer space of smectite in addition to external surfaces, high initial [K] was applied, resulting in low adsorption ratios (Table 1). The low K adsorption ratios make it difficult to distinguish which isotopic fractionation model fit better (Fig. 6), since deviations from linearity would be most apparent in samples with high percentages of sorbed K. Thus, we cannot fully distinguish the mineralogy control on K isotopic fractionation factor based on the present data.

5.1.3. Complexation controls

Two complexation modes may exist on clay surfaces: inner-sphere complexation (chemisorption, with direct bonding to surface sites) and outer-sphere complexation (physisorption, with electrostatic attraction). These two modes may cause different isotopic fractionation, and they are easily differentiated based on the consequence of ionic strength variation because weakly adsorbed cations can be easily replaced with excess Na^+ at high IS (Lützenkirchen, 1997; Wasylenki et al., 2014; Dong and Wasylenki, 2016; Guinoiseau et al., 2016; Li and Liu, 2020). Based on our results, adsorbed K^+ are dominated by outer-sphere complexes since almost all K can be desorbed at high IS at 0.1 and 0.5 M NaCl, regardless of variations in pH and initial [K] (Figs. 3-4). Because our experiments use a wide range of IS from 0.001 to 0.5 M, K adsorption on kaolinite and smectite could be better characterized by the electrostatic attraction between K^+ in water and negatively charged clay surfaces within the pH range (Fig. S2). The occurrence of outer-sphere K is further supported by the K *K*-edge XANES spectra (Fig. 1). In addition to K features of pristine clays, only the features of KCl (s) are identified in the XANES spectra. This is likely caused by the transformation of physically adsorbed $K{\cdot}(H_2O)_6^+$ into solid-state KCl salt after dehydration (drying clays during sample processing) after experiments. We consider this is likely since Cl^- could be tightly complexed to surface Al^{3+} vacancy on clays and may be bounded to surface K^+ as anion-bridged ternary complexes (e.g., ≡Si/Al-Cl-K, Vasconcelos et al., 2007).

A similar complexation mode has also been documented for Cs^+, which is physicochemically similar to K^+ (Durrant et al., 2018). Clay K desorption at high IS is near-complete, implying fully exchangeable adsorption (i.e., outer-sphere complexation) (Table 1). Dissolved K^+ probably has lower affinities for the exchange pool relative to Na^+ and multivalent cations (Appelo, 1996), and surface K^+ complexes are hydrated and readily exchangeable due to low hydration energy (Lee et al., 2017). Brazier et al. (2019) documented fully exchangeable Ca^{2+} sorbed on clays. Because K has a lower Gibbs free energy of hydration and a faster exchange rate with water (10^9•s^{-1}) compared to Ca (10^8•s^{-1}) (Lincoln and Merbach, 1995; Markham et al., 1996; Schott et al., 2009), fully exchangeable K on clay surfaces is expected. In sum, outer-sphere K complexation probably controls the equilibrium isotopic fractionation during clay adsorption.

Here, we correlate the K isotopic fractionation to surface complexation. Major factors modulating equilibrium isotopic fractionation include temperature, relative mass differences between isotopes, and bond stiffness related to bond length and atomic coordination number (Schauble, 2004). In the absence of temperature change, the isotopic fractionation between ^{39}K and ^{41}K is likely modulated by atomic coordination. The same mechanism has been reported for outer-sphere Zn^{2+} on kaolinite, Ca^{2+} hosted in mica interlayer spaces, and Ni^{2+} adsorption on calcite (Guinoiseau et al., 2016; Brazier et al., 2019; Alvarez et al., 2020), producing discernable isotopic fractionations during adsorption. So far, the mechanisms responsible for the fractionation of stable metal isotopes with respect to outer-sphere complexation on clay surfaces remain elusive. It is generally believed that K^+ conserves its hydration sphere with coordination numbers of 6 or 7 based on the hybrid quantum mechanical/molecular studies (Varma and Rempe, 2006; Rowley and Roux, 2012). Although the coordination number of K atoms may not vary when forming outer-sphere complexes, slight distortions of bond length and angle may occur. It is reasonable because water molecules bind to metal ions mainly through ion-dipole bonds of apparent electrostatic characters (Persson, 2010). A general rule for equilibrium isotopic fractionation states that heavier isotopes of an element prefer to concentrate in the species where they form the stiffer bond (Schauble, 2004). Therefore, ionic K^+ in surrounding waters enriched in heavier isotopes should form stiffer (or shorter) K-O bonds compared with surface K complexes.

5.2. Why cannot adsorption experiments reconcile field observation?

5.2.1. Distinct directions of isotopic fractionation

We note that the direction of K isotopic fractionation in the adsorption experiments (heavier K sorbed on clays) is opposite to field observations (lighter K scavenged in clays, S. Li et al., 2019; Chen et al., 2020; Santiago Ramo et al., 2020; Teng et al., 2020; Wang et al., 2020b). From experimental data, isotopically heavy K prefers to be fixed onto clay surface by electrostatic attraction without direct bonding (Fig. 6). By contrast, we consider that K incorporation in clay lattice likely prefers isotopically light K and has marked contributions to observed K isotopic fractionations in weathering environments. Two potential explanations have been proposed for the light K isotopic composition in secondary minerals formed at Earth's surface environments than the Bulk Silicate Earth (BSE, $\delta^{41}K$ of $-0.48 \pm 0.03‰$, Wang and Jacobsen, 2016). First, rate-limiting processes are pervasive for mineral formation at low-temperature geochemical systems (DePaolo, 2011; Watkins et al., 2017). Therefore, it is plausible that kinetic K isotopic signatures can be partially preserved in the lattice of secondary minerals. We may expect that isotopically light K co-precipitate with clays through ion diffusion and/or dehydration (Bourg et al., 2010; Hofmann et al., 2012). Alternatively, isotopically light K in clay structures might be explained by equilibrium isotope processes linked with variations in local atomic coordination. To solve this discrepancy, we stress the importance and discuss the mechanism of structural incorporation in comparison with adsorption responsible for K isotopic fractionation during clay formation based on K XANES of unreacted clays (only primary K in the structure) (Fig. 1b).

5.2.2. Coordination controls

Coordination environment identification can further be obtained from the XANES spectra (Fig. 1). Extracting qualitative structural information, as coordination numbers, from the K *K*-edge XANES is a critical step in extending XAFS studies of low concentration systems. Based on the Random Forest Models, Zheng et al. (2020) suggested that the feature of the pre-edge (1) and dominant peak (2) are the most suitable for such interpretation. The trend line between the K-O coordination number and the intensity ratio of Peak1/Peak2 is shown in Fig. 1b (reported for Fe and Ga XANES, Nishi et al., 1998; Wilke et al., 2001). It predicts that K in clay minerals (e.g., illite, kaolinite, and smectite) situates in higher-coordinated environments compared to those of $KCl_{(aq)}$ and $KCl_{(s)}$. This empirical pattern is consistent with spectral analyses and theoretical calculations (Table S4). The data demonstrate that K is likely fixed into clay lattice of higher coordination numbers compared with K^+ in water (hexacoordination). Therefore, our results suggest a stiffer K-O bonding environment in ionic K in water compared with lattice K.

If K isotopic fractionation follows a thermodynamic equilibrium path during clay incorporation, preferential uptake of isotopically light K is expected based on the stable isotope theory (Schauble, 2004). The K isotopic fractionation is stemmed from coordination differences in aqueous K (stiffer K-O bonds) and structural K (weaker K-O bonds). This pattern agrees with previous reports based on theoretical calculations, suggesting that equilibrium isotopic fractionation between aqueous K^+ and K fixed within illite structure has $\Delta^{41}K_{aq\text{-}illite}$ of 0.24‰ at 25 °C (Zeng et al., 2019). Thus, the importance of clay K incorporation over adsorption in weathering environments could explain the positive K isotopic offset of ~0.6‰ in seawater from the upper continental crust (Hille et al., 2019; Huang et al., 2020; Wang et al., 2020b). In summary, two points need to be emphasized. First, the atomic environments of lattice K, sorbed K, and aqueous K are different, and their bond stiffness of K-O likely follow the order of clay lattice K < aqueous K < sorbed K. Such structural changes can result in the enrichment of lighter K isotopes in clay lattice and heavier isotopes on clay surfaces when equilibrium fractionation is reached. Second, clay structural incorporation and adsorption potentially drive K isotopic fractionation in opposite directions and their contributions should be evaluated. Further clay synthesis experiments as well as atomic coordination analysis are needed to verify these views.

5.3. Geochemical implications

This study improves the understanding of the patterns of K isotopic fractionation on Earth's surface (e.g., soils, rivers, and oceans), where K-containing solutions react with common clay minerals such as kaolinite and smectite. Our experimental results indicate that the isotopic fractionation between aqueous K and adsorbed K is about 0.6–0.8‰ under ambient conditions following the equilibrium isotopic fractionation law ($\alpha_{ad\text{-}aq}$ of 1.00075). Based on our XANES spectra, K is likely bounded onto clays as outer-sphere complexes, susceptible to variations in ionic strength (the presence of competitive cations), and the net isotopic fractionation between sorbed and dissolved K pools is constant. Although K isotopic fractionation during co-precipitation with clay minerals has not been experimentally examined, our K *K*-edge XANES data suggest the higher coordination numbers of structural K compared with K^+ in waters. This is consistent with recent field studies that K removal via co-precipitation with clays is dominated K isotopic fractionation mechanism in nature and clays prefer light K isotopes (Chen et al., 2020; S. Li et al., 2019; Teng et al., 2020)."

By contrast, K adsorption may be critical for soils (or regolith) since there are relatively high proportions of water-soluble and exchangeable K (up to ~100%) in global soils (Pal et al., 1999; Howard et al., 2012), positively correlates with the clay content in depth. Since clay uptake of light K was observed in natural environments (S. Li et al., 2019; Chen et al., 2020; Huang et al., 2020; Teng et al., 2020; Wang et al., 2020a), we consider that most K associated with clays is in the structure of minerals. Despite simplified experimental setup and a less critical role of clay adsorption in nature, our result could be applicable to specific terrestrial environments such as calcareous soils (Griffioen, 2001), given high surface affinity to cations of

clays at high pH. Moreover, a survey of K isotopic composition in river water globally collected show a wide range of $\delta^{41}K$ higher, lighter, or comparable to the composition of the continental crust (Wang et al., 2020a). Hence, the contribution of clay adsorption needs further consideration.

This study contributes to understanding the mass balance in the global oceanic K budget. The experimental data combined with synchrotron-based analyses have confirmed that the opposite K isotopic fractionation patterns are driven by surface adsorption and structural incorporation in clays during chemical weathering and pedogenesis (S. Li et al., 2019; Chen et al., 2020; Huang et al., 2020; Teng et al., 2020). Adsorption of K on clays potentially modifies the K isotopic composition in fluid phases, including rivers, groundwaters, and pore waters, because it is a ubiquitous process on Earth's surface. It should be noted that in rivers with circumneutral pH and low salinities, K can be transported to the oceans as adsorbed phases on colloids and dissolved loads. A large K pool may be transferred to dissolved pools in estuarine mixing zones between freshwater and seawater due to desorption. Supportively, Tipper et al. (2020) reported a great flux of mobile elements (including clay exchangeable Na and K) with sediments into the ocean could be replaced by Ca^{2+}. Therefore, desorption from suspended sediments in estuaries could introduce a considerable flux of K enriched in ^{41}K to the ocean, which needs additional attention.

6. CONCLUSIONS

In this study, we determined the direction, degrees, and mechanisms of K isotopic fractionation during K adsorption on two naturally occurring clay minerals (kaolinite and smectite) in the closed system at room temperature over a range of solute parameters (ionic strength and pH). Our results reveal that heavy K isotopes are preferentially adsorbed on clays. The enrichment of the solution in light K isotopes relative to adsorbed K on clays yields an average fractionation factor between adsorbed and aqueous phases ($\Delta^{41}K_{ad\text{-}aq}$) of ~0.75‰, which could be best described by an equilibrium fractionation mechanism with constant $\alpha_{ad\text{-}aq}$ of 1.00075 in closed systems. Isotopic equilibria could be achieved after 12 hours, and the net isotopic fractionation ($\Delta^{41}K_{ad\text{-}aq}$) does not depend on solute pH, ionic strength, nor starting KCl solution molarity. Ionic K in water was probably bound to clay surfaces as outer-sphere complexes (physically adsorption), which could be easily exchanged with cations with high ionic strength (Na^+ in this study). Although the net isotopic fractionation ($\Delta^{41}K_{ad\text{-}aq}$) keeps near-constant, heavy K isotopic compositions in reacted solutions ($\delta^{41}K_{aq}$) have been observed along with decreases in the percentage of K adsorption at high ionic strength. Therefore, we conclude that differences in the atomic coordination of K on clay surfaces (outer-sphere complexation) and within clay structures might be responsible for the opposite directions of K isotopic fractionation between clay adsorption experiments and field observations. We also highlight the difference in K isotopic fractionation between clay structural incorporation and surface adsorption during chemical weathering.

Declaration of Competing Interest

The authors declare that they have no known competing financial interests or personal relationships that could have appeared to influence the work reported in this paper.

ACKNOWLEDGMENTS

The authors acknowledge funding support from the NSF Career Award (EAR-1848153) to X.-M. Liu and the Martin Research Fellowship from the University of North Carolina, Chapel Hill to W.S. Li. The authors thank Oleg S Pokrovsky for editorial handling and insightful feedback from Emmanuel Tertre and two anonymous reviewers whose comments helped us improve the manuscript. The authors thank Xikai Wang, Mohsen Shakouri, and Qunfeng Xiao for their help with the XAFS analysis and fruitful discussion. The K *K*-edge XANES spectra provided in this study were collected at Canadian Light Source (CLS), with the approval of the proposal review committee (No. 30G09959 and 32GU010898). CLS is supported by the Canada Foundation for Innovation, Natural Sciences and Engineering Research Council of Canada, University of Saskatchewan, Government of Saskatchewan, Western Economic Diversification Canada, National Research Council Canada, and Canadian Institutes of Health Research.

APPENDIX A. SUPPLEMENTARY MATERIAL

Supplementary data to this article can be found online at https://doi.org/10.1016/j.gca.2021.04.027.

REFERENCES

Amiotte Suchet P., Probst J. L. and Ludwig W. (2003) Worldwide distribution of continental rock lithology: Implications for the atmospheric/soil CO_2 uptake by continental weathering and alkalinity river transport to the oceans. *Global Biogeochem. Cycles* **17**, 1038.

Anbar A. D. and Rouxel O. (2007) Metal stable isotopes in paleoceanography. *Annu. Rev. Earth Planet. Sci.* **35**, 717–746.

Au P. I. and Leong Y. K. (2013) Rheological and zeta potential behaviour of kaolin and bentonite composite slurries. *Colloids Surfaces A Physicochem. Eng. Asp.* **436**, 530–541.

Alvarez C. C., Quitté G., Schott J. and Oelkers E. H. (2020) Experimental determination of Ni isotope fractionation during Ni adsorption from an aqueous fluid onto calcite surfaces. *Geochim. Cosmochim. Acta* **273**, 26–36.

Appelo C. A. J. (1996). Multicomponent ion exchange and chromatography in natural systems, Ch. 4. P.C. Lichtner, C.I. Steefel, E.H. Oelkers (Eds.), Reactive Transport in Porous Media, Reviews in Mineralogy, vol. 34, Mineralogical Society of America, Washington, DC. pp. 193-227.

Balistrieri L. S., Borrok D. M., Wanty R. B. and Ridley W. I. (2008) Fractionation of Cu and Zn isotopes during adsorption onto amorphous Fe(III) oxyhydroxide: Experimental mixing of acid rock drainage and ambient river water. *Geochim. Cosmochim. Acta* **72**, 311–328.

Bryan A. L., Dong S., Wilkes E. B. and Wasylenki L. E. (2015) Zinc isotope fractionation during adsorption onto Mn oxyhydroxide at low and high ionic strength. *Geochim. Cosmochim. Acta* **157**, 182–197.

Brazier J. M., Schmitt A. D., Gangloff S., Pelt E., Chabaux F. and Tertre E. (2019) Calcium isotopic fractionation during adsorp-

tion onto and desorption from soil phyllosilicates (kaolinite, montmorillonite and muscovite). *Geochim. Cosmochim. Acta* **250**, 324–347.
Berner K. and Berner R. A. (2012) *Global environment: Water, air, and geochemical cycles*. Princeton University Press.
Berry A. J. and O'Neill H. S. C. (2004) A XANES determination of the oxidation state of chromium in silicate glasses. *Am. Mineral.* **89**(5–6), 790–798.
Bourg I. C., Richter F. M., Christensen J. N. and Sposito G. (2010) Isotopic mass dependence of metal cation diffusion coefficients in liquid water. *Geochim. Cosmochim. Acta* **74**(8), 2249–2256.
Chen H., Liu X. M. and Wang K. (2020) Potassium isotope fractionation during chemical weathering of basalts. *Earth Planet. Sci. Lett.*, 539.
Chen H., Tian Z., Tuller-Ross B., Korotev R. L. and Wang K. (2019) High-precision potassium isotopic analysis by MC-ICP-MS: An inter-laboratory comparison and refined K atomic weight. *J. Anal. At. Spectrom.* **34**, 160–171.
Christensen J. N., Qin L., Brown S. T. and Depaolo D. J. (2018) Potassium and calciumisotopic fractionation by plants (Soybean [Glycine max], rice [Oryza sativa], and wheat [Triticum aestivum]). *ACS Earth Sp. Chem.* **2**, 745–752.
Calvin S. (2013) *XAFS for Everyone*. CRC Press.
Chaudhuri S., Clauer N. and Semhi K. (2007) Plant decay as a major control of river dissolved potassium: a first estimate. *Chem. Geol.* **243**(1–2), 178–190.
Cibin G., Mottana A., Marcelli A. and Brigatti M. F. (2005) Potassium coordination in trioctahedral micas investigated by K-edge XANES spectroscopy. *Mineral. Petrol.* **85**, 67–87.
Dong S. and Wasylenki L. E. (2016) Zinc isotope fractionation during adsorption to calcite at high and low ionic strength. *Chem. Geol.* **447**, 70–78.
DePaolo D. J. (2011) Surface kinetic model for isotopic and trace element fractionation during precipitation of calcite from aqueous solutions. *Geochim. Cosmochim. Acta* **75**, 1039–1056.
Durrant C. B., Begg J. D., Kersting A. B. and Zavarin M. (2018) Cesium sorption reversibility and kinetics on illite, montmorillonite, and kaolinite. *Sci. Total Environ.* **610–611**, 511–520.
Griffioen J. (2001) Potassium adsorption ratios as an indicator for the fate of agricultural potassium in groundwater. *J. Hydrol.* **254**, 244–254.
Goldberg T., Archer C., Vance D. and Poulton S. W. (2009) Mo isotope fractionation during adsorption to Fe (oxyhydr) oxides. *Geochim. Cosmochim. Acta* **73**(21), 6502–6516.
Guinoiseau D., Gélabert A., Moureau J., Louvat P. and Benedetti M. F. (2016) Zn isotope fractionation during dorption onto kaolinite. *Environ. Sci. Technol.* **50**, 1844–1852.
Gu C., Hart S. C., Turner B. L., Hu Y., Meng Y. and Zhu M. (2019) Aeolian dust deposition and the perturbation of phosphorus transformations during long-term ecosystem development in a cool, semi-arid environment. *Geochim. Cosmochim. Acta* **246**, 498–514.
Geng G., Shi Z., Leemann A., Borca C., Huthwelker T., Glazyrin K., Pekov I. V., Churakov S., Lothenbach B., Dähn R. and Wieland E. (2020) Atomistic structure of alkali-silica reaction products refined from X-ray diffraction and micro X-ray absorption data. *Cem. Concr. Res.* **129**.
Glezakou V. A., Chen Y., Fulton J. L., Schenter G. K. and Dang L. X. (2006) Electronic structure, statistical mechanical simulations, and EXAFS spectroscopy of aqueous potassium. *Theor. Chem. Acc.* **115**, 86–99.
Greaves G. N., Gurman S. J., Catlow C. R. A., Chadwick A. V., Houde-Walter S., Henderson C. M. B. and Dobson B. R. (1991) A structural basis for ionic diffusion in oxide glasses. *Philos. Mag. A Phys. Condens. Matter, Struct. Defects Mech. Prop.* **64**, 1059–1072.
Hu Y., Chen X. Y., Xu Y. K. and Teng F. Z. (2018) High-precision analysis of potassium isotopes by HR-MC-ICPMS. *Chem. Geol.* **493**, 100–108.
Hu Y., Teng F. Z., Plank T. and Chauvel C. (2020) Potassium isotopic heterogeneity in subducting oceanic plates. *Sci. Adv.* **6** (49), eabb2472.
Hu Y., Teng F. Z. and Chauvel C. (2021) Potassium isotopic evidence for sedimentary input to the mantle source of Lesser Antilles lavas. *Geochim. Cosmochim. Acta* **295**, 98–111.
Huang T. Y., Teng F. Z., Rudnick R. L., Chen X. Y., Hu Y., Liu Y. S. and Wu F. Y. (2020) Heterogeneous potassium isotopic composition of the upper continental crust. *Geochim. Cosmochim. Acta* **278**, 122–136.
Hille M., Hu Y., Huang T. Y. and Teng F. Z. (2019) Homogeneous and heavy potassium isotopic composition of global oceans. *Sci. Bull.* **64**, 1740–1742.
Hu Y. F., Coulthard I., Chevrier D., Wright G., Igarashi R., Sitnikov A., Yates B. W., Hallin E. L., Sham T. K. and Reininger R. (2010) Preliminary commissioning and performance of the soft x-ray micro-characterization beamline at the Canadian light source. In *AIP Conference Proceedings*, pp. 343–346.
Hofmann A. E., Bourg I. C. and DePaolo D. J. (2012) Ion desolvation as a mechanism for kinetic isotope fractionation in aqueous systems. *Proc. Natl. Acad. Sci. U S A* **109**(46), 18689–18694.
Howard J. L., Clawson C. R. and Daniels W. L. (2012) A comparison of mineralogical techniques and potassium adsorption isotherm analysis for relative dating and correlation of Late Quaternary soil chronosequences. *Geoderma* **179–180**, 81–95.
Huffman G. P., Huggins F. E., Shoenberger R. W., Walker J. S., Lytle F. W. and Greegor R. B. (1986) Investigation of the structural forms of potassium in coke by electron microscopy and X-ray absorption spectroscopy. *Fuel* **65**, 621–632.
Johnson C. M., Beard B. L. and Albarède F. (2004) Overview and general concepts. *Rev. Mineral. Geochem.* **55**(1), 1–24.
Kump L. R., Brantley S. L. and Arthur M. A. (2000) Chemical weathering, atmospheric CO_2, and climate. *Annu. Rev. Earth Planet. Sci.* **28**, 611–667.
Kosmulski M. (2011) The pH-dependent surface charging and points of zero charge. V. Update. *J. Colloid Interface Sci.* **353**, 1–15.
Kamijo N., Handa K. and Umesaki N. (1996) Soft x-ray xafs studies on the local structure of K_2O-SiO_2 glasses. *Mater. Trans. JIM* **37**, 927–931.
Lee J., Park S. M., Jeon E. K. and Baek K. (2017) Selective and irreversible adsorption mechanism of cesium on illite. *Appl. Geochem.* **85**, 188–193.
Li C. and Yang S. (2010) Is chemical index of alteration (CIA) a reliable proxy for chemical weathering in global drainage basins? *Am. J. Sci.* **310**(2), 111–127.
Liu X. M., Rudnick R. L., McDonough W. F. and Cummings M. L. (2013) Influence of chemical weathering on the composition of the continental crust: Insights from Li and Nd isotopes in bauxite profiles developed on Columbia River Basalts. *Geochim. Cosmochim. Acta* **115**, 73–91.
Li W., Beard B. L. and Li S. (2016) Precise measurement of stable potassium isotope ratios using a single focusing collision cell multi-collector ICP-MS. *J. Anal. At. Spectrom.* **31**, 1023–1029.
Li X., Han G., Zhang Q. and Miao Z. (2020a) Optimal separation method for high-precision K isotope analysis by using MC-ICP-MS with a dummy bucket. *J. Anal. At. Spectrom.* **35**, 1330–1339.

Li S., Li W., Beard B. L., Raymo M. E., Wang X., Chen Y. and Chen J. (2019) K isotopes as a tracer for continental weathering and geological K cycling. *Proc. Natl. Acad. Sci. U. S. A.* **116**, 8740–8745.

Liu H., Wang K., Sun W. D., Xiao Y., Xue Y. Y. and Tuller-Ross B. (2020) Extremely light K in subducted low-T altered oceanic crust: Implications for K recycling in subduction zone. *Geochim. Cosmochim. Acta* **277**, 206–223.

Li D., Liu S. A. and Li S. (2015) Copper isotope fractionation during adsorption onto kaolinite: Experimental approach and applications. *Chem. Geol.* **396**, 74–82.

Li W. and Liu X. M. (2020) Experimental investigation of lithium isotope fractionation during kaolinite adsorption: Implications for chemical weathering. *Geochim. Cosmochim. Acta* **284**, 156–172.

Li W., Liu X. M. and Hu Y. (2020b) Potassium and Calcium K-Edge XANES in Chemical Compounds and Minerals: Implications for Geological Phase Identification. *Geostandards Geoanalytical Res.* **44**(4), 805–819.

Li W., Liu X. M., Wang K. and Koefoed P. (2021a) Lithium and potassium isotope fractionation during silicate rock dissolution: An experimental approach. *Chem. Geol.* **568** 120142.

Li W., Liu X. M., Wang K., Fodrie J., Yoshimura T. and Hu Y. (2021b) Potassium phases and isotopic composition in modern marine biogenic carbonates. *Geochim. Cosmochim. Acta*. https://doi.org/10.1016/j.gca.2021.04.018 (in press).

Lützenkirchen J. (1997) Ionic strength effects on cation sorption to oxides: Macroscopic observations and their significance in microscopic interpretation. *J. Colloid Interface Sci.* **195**, 149–155.

Lincoln S. F. and Merbach A. E. (1995) Substitution reactions of solvated metal ions. In *Advances in Inorganic Chemistry* (ed. A. G. Sykes). Academic Press, pp. 1–88.

Morgan L. E., Santiago Ramos D. P., Davidheiser-Kroll B., Faithfull J., Lloyd N. S., Ellam R. M. and Higgins J. A. (2018) High-precision $^{41}K/^{39}K$ measurements by MC-ICP-MS indicate terrestrial variability of: $\delta^{41}K$. *J. Anal. At. Spectrom.* **33**, 175–186.

Moynier F., Hu Y., Wang K., Zhao Y., Gérard Y., Deng Z., Moureau J., Li W., Simon J. I. and Teng F. Z. (2021) Potassium isotopic composition of various samples using a dual-path collision cell-capable multiple-collector inductively coupled plasma mass spectrometer, Nu instruments Sapphire. *Chem. Geol.*, 120144.

Michalopoulos P. and Aller R. C. (1995) Rapid clay mineral formation in Amazon delta sediments: reverse weathering and oceanic elemental cycles. *Science* **270**(5236), 614–617.

Miller D. G., Ting A. W., Rard J. A. and Eppstein L. B. (1986) Ternary diffusion coefficients of the brine systems NaCl (0.5 M)-Na_2SO_4 (0.5 M)-H_2O and NaCl (0.489 M)-$MgCl_2$ (0.051 M)-H_2O (seawater composition) at 25°C. *Geochim. Cosmochim. Acta* **50**, 2397–2403.

Markham G. D., Glusker J. P., Bock C. L., Trachtman M. and Bock C. W. (1996) Hydration energies of divalent beryllium and magnesium ions: An ab initio molecular orbital study. *J. Phys. Chem.* **100**(9), 3488–3497.

Nielsen S. G., Wasylenki L. E., Rehkämper M., Peacock C. L., Xue Z. and Moon E. M. (2013) Towards an understanding of thallium isotope fractionation during adsorption to manganese oxides. *Geochim. Cosmochim. Acta* **117**, 252–265.

Nishi K., Shimizu K. I., Takamatsu M., Yoshida H., Satsuma A., Tanaka T., Yoshida S. and Hattori T. (1998) Deconvolution analysis of Ga K-Edge XANES for quantification of gallium coordinations in oxide environments. *J. Phys. Chem. B* **102**, 10190–10195.

Parendo C. A., Jacobsen S. B. and Wang K. (2017) K isotopes as a tracer of seafloor hydrothermal alteration. *Proc. Natl. Acad. Sci. U. S. A.* **114**, 1827–1831.

Pal Y., Wong M. T. F. and Gilkes R. J. (1999) The forms of potassium and potassium adsorption in some virgin soils from south-western Australia. *Aust. J. Soil Res.* **37**, 695–709.

Pokrovsky O. S., Viers J. and Freydier R. (2005) Zinc stable isotope fractionation during its adsorption on oxides and hydroxides. *J. Colloid Interface Sci.* **291**(1), 192–200.

Persson I. (2010) Hydrated metal ions in aqueous solution: How regular are their structures? *Pure Appl. Chem.* **82**(10), 1901–1917.

Rowley C. N. and Roux B. (2012) The solvation structure of Na^+ and K^+ in liquid water determined from high level ab initio molecular dynamics simulations. *J. Chem. Theory Comput.* **8**(10), 3526–3535.

Rudnick R. L. and Gao S. (2013) Composition of the continental crust. In Treatise on Geochemistry: Second Edition Elsevier Inc. pp. 1–51.

Rahman S. Reverse weathering reactions in marine sediments (2019) In Encyclopedia of Ocean Science: third edition Academic Press, Oxford. pp. 216-227

Reinholdt M. X., Hubert F., Faurel M., Tertre E., Razafitianamaharavo A., Francius G., Prêt D., Petit S., Béré E., Pelletier M. and Ferrage E. (2013) Morphological properties of vermiculite particles in size-selected fractions obtained by sonication. *Appl. Clay Sci.* **77–78**, 18–32.

Ravel B. and Newville M. (2005) ATHENA, ARTEMIS, HEPHAESTUS: Data analysis for X-ray absorption spectroscopy using IFEFFIT. *J. Synchrotron Radiation* **12**, 537–541.

Roberts J., Kaczmarek K., Langer G., Skinner L. C., Bijma J., Bradbury H., Turchyn A. V., Lamy F. and Misra S. (2018) Lithium isotopic composition of benthic foraminifera: A new proxy for paleo-pH reconstruction. *Geochim. Cosmochim. Acta* **236**, 336–350.

Sardans J. and Peñuelas J. (2015) Potassium: A neglected nutrient in global change. *Glob. Ecol. Biogeogr.* **24**, 261–275.

Santiago Ramos D. P., Morgan L. E., Lloyd N. S. and Higgins J. A. (2018) Reverse weathering in marine sediments and the geochemical cycle of potassium in seawater: Insights from the K isotopic composition ($^{41}K/^{39}K$) of deep-sea pore-fluids. *Geochim. Cosmochim. Acta* **236**, 99–120.

SantiagoRamos D. P., Coogan L. A., Murphy J. G. and Higgins J. A. (2020) Low-temperature oceanic crust alteration and the isotopic budgets of potassium and magnesium in seawater. *Earth Planet. Sci. Lett.* **541** 116290.

Sun Y., Teng F. Z., Hu Y., Chen X. Y. and Pang K. N. (2020) Tracing subducted oceanic slabs in the mantle by using potassium isotopes. *Geochim. Cosmochim. Acta* **278**, 353–360.

Spivak-Birndorf L. J., Wang S. J., Bish D. L. and Wasylenki L. E. (2018) Nickel isotope fractionation during continental weathering. *Chem. Geol.* **476**, 316–326.

Simonsson M., Bergholm J., Lemarchand D. and Hillier S. (2016) Mineralogy and biogeochemistry of potassium in the Skogaby experimental forest, southwest Sweden: pools, fluxes and K/Rb ratios in soil and biomass. *Biogeochemistry* **131**(1), 77–102.

Schoonheydt R. A. and Johnston C. T. (2006) Surface and interface chemistry of clay minerals. In Handbook of Clay Science (Eds), vol. 1, Elsevier. pp. 87-113.

Schott J., Pokrovsky O. S. and Oelkers E. H. (2009) The link between mineral dissolution/precipitation kinetics and solution chemistry. *Rev. Mineral. Geochem.* **70**(1), 207–258.

Schauble E. A. (2004) Applying stable isotope fractionation theory to new systems. *Rev. Mineral. Geochemistry* **55**, 65–111.

Spiro C. L., Wong J., Lytle F. W., Greegor R. B., Maylotte D. H. and Lamson S. H. (1986) Forms of potassium in coal and its combustion products. *Fuel* **65**, 327–336.

Tripler C. E., Kaushal S. S., Likens G. E. and Todd Walter M. (2006) Patterns in potassium dynamics in forest ecosystems. *Ecol. Lett.* **9**, 451–466.

Teng F. Z., Dauphas N. and Watkins J. M. (2017) Non-traditional stable isotopes: retrospective and prospective. *Reviews Mineral. Geochem.* **82**(1), 1–26.

Teng F. Z., Hu Y., Ma J. L., Wei G. J. and Rudnick R. L. (2020) Potassium isotope fractionation during continental weathering and implications for global K isotopic balance. *Geochim. Cosmochim. Acta* **278**, 261–271.

Tipper E. T. Stevenson E. I., Alcock V., Knight A. C., Baronas J. J., Hilton R. G., Bickle M. J., Larkin C. S., Feng L., Reelph K. E. and Hughes G. Global silicate weathering flux overestimated because of sediment–water cation exchange. Proc. Natl. Acad. Sci. U. S. A. 118(1). e2016430118.

Uddin M. K. (2017) A review on the adsorption of heavy metals by clay minerals, with special focus on the past decade. *Chem. Eng. J.* **308**, 438–462.

Varma S. and Rempe S. B. (2006) Coordination numbers of alkali metal ions in aqueous solutions. *Biophys. Chem.* **124**, 192–199.

Vasconcelos I. F., Bunker B. A. and Cygan R. T. (2007) Molecular dynamics modeling of ion adsorption to the basal surfaces of kaolinite. *J. Phys. Chem. C* **111**(18), 6753–6762.

Wang K. and Jacobsen S. B. (2016) An estimate of the Bulk Silicate Earth potassium isotopic composition based on MC-ICPMS measurements of basalts. *Geochim. Cosmochim. Acta* **178**, 223–232.

Wang K., Peucker-Ehrenbrink B., Chen H., Lee H. and Hasenmueller E. A. (2020a) Dissolved potassium isotopic composition of major world rivers. *Geochim. Cosmochim. Acta* **294**, 145–159.

Wang K., Close H. G., Tuller-Ross B. and Chen H. (2020b) Global average potassium isotope composition of modern seawater. *ACS Earth Space Chem.* **4**(7), 1010–1017.

Wasylenki L. E., Swihart J. W. and Romaniello S. J. (2014) Cadmium isotope fractionation during adsorption to Mn oxyhydroxide at low and high ionic strength. *Geochim. Cosmochim. Acta* **140**, 212–226.

Wasylenki L. E., Schaefer A. T., Chanda P. and Farmer J. C. (2020) Invited research article Differential behavior of tungsten stable isotopes during sorption to Fe versus Mn oxyhydroxides at low ionic strength. *Chem. Geol.* **140**, 212–226.

Watkins J. M., DePaolo D. J. and Watson E. B. (2017) Kinetic fractionation of non-traditional stable isotopes by diffusion and crystal growth reactions. In *Non-Traditional Stable Isotopes*. Walter de Gruyter GmbH, pp. 85–126.

Wilke M., Farges F., Petit P. E., Brown G. E. and Martin F. (2001) Oxidation state and coordination of Fe in minerals: An Fe K-XANES spectroscopic study. *Am. Mineral.* **86**, 714–730.

Xu W., Chen D., Chu W., Wu Z., Marcelli A., Mottana A., Soldatov A. and Brigatti M. F. (2011) Quantitative local structure determination in mica crystals: Ab initio simulations of polarization XANES at the potassium K-edge. *J. Synchrotron Radiat.* **18**, 418–426.

Xu W., Zhu J. M., Johnson T. M., Wang X., Lin Z. Q., Tan D. and Qin H. (2020) Selenium isotope fractionation during adsorption by Fe, Mn and Al oxides. *Geochim. Cosmochim. Acta* **272**, 121–136.

Xu Y. K., Hu Y., Chen X. Y., Huang T. Y., Sletten R. S., Zhu D. and Teng F. Z. (2019) Potassium isotopic compositions of international geological reference materials. *Chem. Geol.* **513**, 101–107.

Yuan W., Saldi G. D., Chen J. Bin, Vetuschi Zuccolini M., Birck J. L., Liu Y. and Schott J. (2018) Gallium isotope fractionation during Ga adsorption on calcite and goethite. Geochim. Cosmochim. Acta 223, 350–363.

Zeng H., Rozsa V. F., Nie N. X., Zhang Z., Pham T. A., Galli G. and Dauphas N. (2019) Ab initio calculation of equilibrium isotopic fractionations of potassium and rubidium in minerals and water. *ACS Earth Sp. Chem.* **3**, 2601–2612.

Zheng C., Chen C., Chen Y. and Ong S. P. (2020) Random forest models for accurate identification of coordination environments from X-ray absorption near-edge structure. *Patterns* **1** 100013.

Associate editor: Oleg Pokrovsky